JOM
https://doi.org/10.1007/s11837-026-08388-1
© 2026 The Author(s)

Numerical Investigation of Titanium Particle Temperature Control via Feeding Gas Flow Rate in an RF Induction Plasma System

İRFAN ÜNAL ,[1,2,3] RAHMI ÜNAL,[1] and MURAT ERBAŞ[1]

1.—Engineering Faculty, Mechanical Engineering Department, Gazi University, Ankara, Turkey.
2.—Graduate School of Natural and Applied Sciences, Gazi University, Ankara, Turkey.
3.—e-mail: irfanunal@gazi.edu.tr

Plasma spheroidization is used to transform irregularly shaped metal and ceramic powders into spherical forms and to recycle and spheroidize the used powders. The inductively coupled radiofrequency (RF) plasma system is used for spheroidization of irregularly shaped particles. In this study, a computational fluid dynamics (CFD) model is developed for a radiofrequency plasma system designed for powder spheroidization. The electric field is generated analytically by solving the RF coil system, and the resulting equations are then implemented as user-defined functions (UDFs) within the CFD model. UDF codes were created and defined in the Fluent program to generate RF plasma. Electromagnetic fields and fluid flow have been modeled numerically, yielding temperature and velocity distributions. The effect of this plasma environment on the temperature of titanium particles is investigated using various particle-feeding gas flow rates. As a result, an optimal powder feeding rate can be determined. It was observed that high particle velocities prevent the attainment of the required melting temperature, whereas low velocities may cause the temperature to exceed the boiling point. These results indicate that the feeding gas flow rate can be determined for a specific powder size range to achieve powder temperatures within the powder's melting and boiling ranges.

INTRODUCTION

In recent decades, the development of additive manufacturing (AM) technologies has enabled the production of complex parts at a low cost and high efficiency.[1–3] AM is used to manufacture 3D objects layer by layer from digital models, eliminating the need for additional tools.[4] In recent years, laser powder bed fusion (LPBF) has emerged as an AM technique for producing complex parts.[5] Using metal powder with the desired physical and chemical properties is essential for powder-bed methods. Spherical powders are preferred as raw materials over irregularly shaped powders[6] because of their superior powder flowability. The inductively coupled plasma (ICP) system could be used to spheroidize irregularly shaped powders. After the powder spheroidization process, the apparent and true densities of the powders increase significantly.[7] The inductively coupled plasma spheroidization system uses radiofrequency (RF) induction coils to produce high-temperature plasma. The induction coils induce electromagnetic fields in the center of the plasma torch. A comprehensive review of ICP studies in the literature shows that most are experimental.

RF plasma spheroidization is preferred for spheroidization metals and ceramics with high melting points. This process plays a critical role in industrial and scientific applications. It is applied to alter the physical and chemical properties of powders, improve processing methods, and enhance product quality.[8] RF plasma technology offers innovative and effective solutions.[9,10] RF plasma

(Received December 23, 2025; accepted April 21, 2026)

Published online: 10 June 2026

systems typically operate at specific radiofrequencies, such as 3–6 MHz,[11–13] which are selected to optimize plasma formation. RF energy accelerates electrons in the plasma to high energies, enabling precise control over the plasma's properties. This capability makes RF plasma systems an ideal choice for numerous industrial processes. Significantly, the RF plasma system enables the spheroidization of non-spherical powders and allows damaged or distorted powders to be spheroidized through recycling. This process helps reduce powder costs and prevents waste.[14]

Numerous studies have reported that the plasma environment used for powder spheroidization must be ≥ 10,000 K.[15–17] Critical parameters for effective plasma generation include RF frequency, power level, and gas flow rate. Optimizing these parameters enhances plasma quality and improves the efficiency of the powder spheroidization process.[18–20] Once the plasma is generated, irregularly shaped powders are introduced into the plasma field with a carrier gas. As the powders pass through the high-temperature zone, they are partially or completely melted at their surfaces.[21] Upon exiting the plasma region, the temperature gradient induces high surface tension, facilitating the spheroidization of the powders.[22] Among plasma parameters, the flow rates of the gases supplied to the torch are among the most critical factors influencing plasma formation, temperature distribution, particle residence time within the plasma, and particle spheroidization.[23,24]

The number of numerical studies is limited, and they generally focus only on modeling the plasma environment. Modeling studies of powder passing through the ICP torch are few,[11,12,25–28] and it is assumed that no temperature gradient occurs within the particle cross-section.[11,12,29] By explicitly modeling these internal gradients, this study achieves precise thermal control over the spheroidization process. While typical AM powders range from 15 to 150 μm, this work focuses on 400 μm Ti particles as a worst-case scenario to evaluate the maximum thermal processing limits of the 125-kW RF plasma system. Spheroidizing such coarse particles is crucial for specialized industrial applications, including the recycling of distorted non-standard feedstock and the fabrication of porous orthopedic coatings where standard fine powders do not meet specific thickness or porosity requirements. Furthermore, this study provides a quantified process window for high-power (125 kW) plasma spheroidization of coarse powders (400 μm), addressing a significant gap in the literature that predominantly focuses on low-power systems and fine particles.

In the literature, CFD analysis has been conducted using tools such as Comsol, Fluent,[12] and OpenFOAM.[27] However, these modeling and analysis approaches come with certain limitations and challenges. This analytical approach is inherently a mesoscale problem. Macroscale finite element and finite volume CFD codes are incapable of modeling molecular groups, owing to the continuum assumption. Therefore, in our analysis, UDF (User-Defined Function) codes were utilized in the Fluent CFD model, with a primary focus on the electric field, and simulations were performed accordingly.[30] UDF codes were created and defined in the Fluent program to generate RF plasma in the torch. Electromagnetic fields and fluid flow have been modeled numerically, and temperature and velocity distributions have been obtained within the torch. The effect of this plasma environment on the temperature of titanium particles was determined and discussed using various particle-feeding gas flow rates.

NUMERICAL MODEL

In this study, the analysis work is divided into two groups. The first group involves studies on RF plasma generation. In this case, no particles are present within the plasma; only the plasma environment is created. Various gas flow rates were used in these analyses, and the results are reported in the paper. The second group examines the effect of the temperature distribution obtained in the first analysis on the powder particles. This section discusses the temperature distribution within powder particles as they move at varying speeds in the plasma environment to determine the carrier gas flow rate.

In analysis work, the plasma is assumed to be in local thermodynamic equilibrium and optically thin. It is also assumed that the ICP plasma torch operates under constant atmospheric pressure. The effects of titanium powder on viscosity and electrical conductivity are neglected. In the modeling, argon gas is chosen for the sheath, plasma, and carrier gas. The flow is modeled in a steady state, neglecting transient effects in the flow field. The reason for choosing argon gas in the modeling study is its ability to ionize efficiently, low cost, chemical inertness, and widespread preference over other gases for plasma generation, as indicated in experimental studies in the literature.[31,32] In the modeling studies, the properties of argon gas, such as thermal conductivity, electrical conductivity, and specific heat, have been formulated as equations and implemented in the CFD program as a User-Defined Function (UDF).[33,34]

The torch geometry used in the analysis was selected based on the study conducted by Nam et al.[11] The torch geometry employed in our analysis is shown in Fig. 1. The dimensions of the given geometry and the simulation parameters are provided in Table I.

Plasma Equations and Boundary Conditions

Mathematical approaches are employed to create a radiofrequency-excited plasma environment and

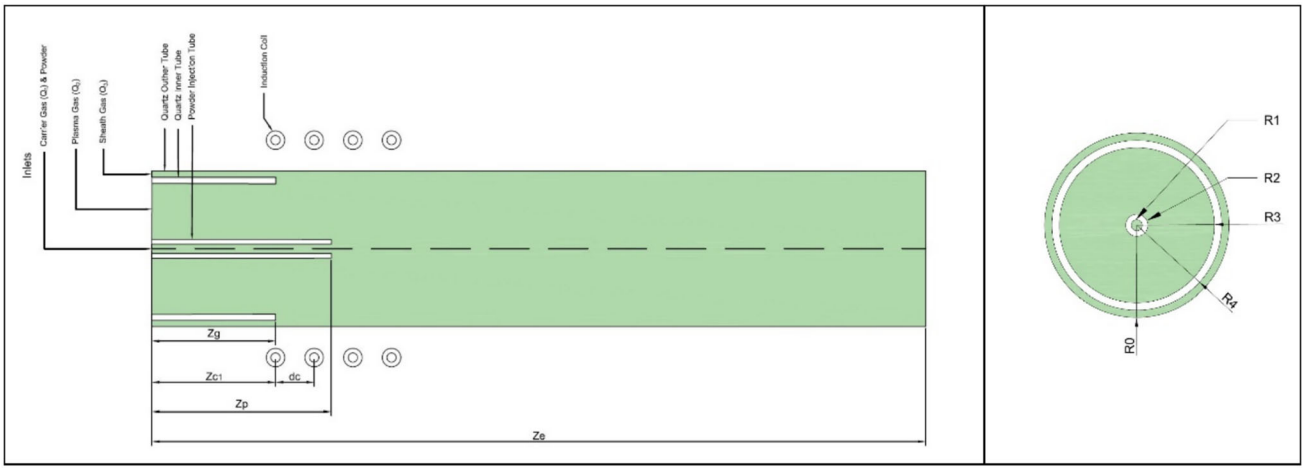


Fig. 1. Geometry of the torch used in this study.

Table I. Design and simulation parameters used in simulation studies

Parameters	Value	Unit
RF power input (P_{RF})	125	kW
Number of RF coil turns (n)	4	Times
Oscillator frequency (f)	4	MHz
Inner radius of injection probe (R_1)	1.5	mm
Outer radius of dtion probe (R_2)	3.0	mm
Inner radius of gas guide (R_3)	21.0	mm
Outer radius of gas guide (R_4)	23.0	mm
Inner radius of plasma confinement tube (R_0)	25.0	mm
Axial position of the torch exit (Ze = L)	250.0	mm
Axial position of gas guide tip (Zg)	40	mm
Distance of induction probe (Zp)	58	mm
Distance between coil turns (dc)	12.5	mm
Axial position of the first coil turn (Zc_1)	40.0	mm

to simulate the effect of its temperature on powder particles passing through it. The single-medium approach is favorable for computational economy at very low powder density (alpha volume fraction < 0.01). In our RF plasma modeling, essential factors such as plasma frequency, excitation effects, and heat transfer have been calculated by considering the properties of plasma carriers, including temperature, density, and velocity distributions. Continuity, momentum, and total energy equations have been utilized in these modeling processes. The resulting equations have been integrated into the CAD model as UDF.

Continuity equation:

$$\vec{\nabla} \cdot (\rho \vec{v}) = 0 \tag{1}$$

Equation 1 is the steady-state continuity equation for compressible fluids, ρ is density, and $\vec{v}$ is the velocity vector.

Momentum equation:

$$\underset{\text{I}}{\vec{\nabla} \cdot (\rho \vec{v} \vec{v})} = \underset{\text{II}}{-\vec{\nabla} p} + \vec{\nabla} \cdot \underset{\text{III}}{\left\{ \mu \left[\left(\vec{\nabla} \vec{v} + \vec{\nabla} \vec{v}^T \right) - \frac{2}{3} \delta \vec{\nabla} \cdot \vec{v} \right] \right\}} + \underset{\text{IV}}{(q \vec{v}_p) \times \left(\vec{\nabla} \times \vec{A} \right)} \tag{2}$$

$$q \vec{v}_p = \vec{j} = -\sigma \frac{\partial \vec{A}}{\partial t} \tag{3}$$

Equation 2 is the momentum equation for laminar flows. P is pressure, μ is viscosity, and $\vec{A}$ is the magnetic vector potential. Term **I** refers to momentum convection between cells. Term **II** is the effect of the pressure gradient. Term **III** is the effect of viscosity on cells. Term **IV** is the Lorentz force. The last term in Eq. 2 is rearranged using Eq. 3 to incorporate the effect of the induced current by RF coils.q is the particle charge, $\vec{v}_p$ is the particle velocity, $\vec{j}$ is the current density vector, and σ is the electrical conductivity.

Total energy equation:

$$\vec{\nabla}\cdot(\vec{v}(\rho e_T + p)) = \underset{\text{I}}{\vec{\nabla}\cdot} \left\{ k\vec{\nabla}T + \vec{v}\cdot\left(\mu\left[\left(\vec{\nabla}\vec{v} + \vec{\nabla}\vec{v}^T\right) - \frac{2}{3}\delta\vec{\nabla}\cdot\vec{v}\right]\right)\right\}_{\text{III}} + \sigma\left(\frac{\partial\vec{A}}{\partial t}\cdot\frac{\partial\vec{A}}{\partial t}\right)_{\text{IV}} \quad (4)$$

Equation 4 is the total internal energy equation. Term **I** represents energy convection and pressure work. Term **II** is the heat conduction term. Term **III** is viscous dissipation. Term **IV** is Joule heating. The Lorentz force term does not appear in the energy equation because the flow velocity and Lorentz force are perpendicular. e_T is the total internal energy, and k is the thermal conductivity.

Magnetic vector potential solution for N coils:

$$\vec{A}(\vec{r},t) = \sum_{i=1}^{N}\frac{\mu_0}{4\pi}\int_0^{2\pi}\frac{\vec{j}\sin(wt)}{\left|\vec{r}-\overrightarrow{r_{c,i}}\right|}d\theta \quad (5)$$

The induced magnetic field of coils at a specified point is calculated using Eq. 5. *Thepositionvectorsr* and $\overrightarrow{r_{c,i}}$ are position vectors of the calculation and coil differential element. μ_0 is vacuum magnetic permeability, and w is the angular speed of the alternating current. The integral has been calculated using Fejèr quadrature. In this computation, the integral was evaluated with ten quadrature points. The coils were considered a two-dimensional circle in the calculation of this integral, and the results of the integrals were summed for each turn. In the computations performed using the flow rate values for our system, as presented in Table II, the Reynolds numbers are < 2000. Consequently, the flow regime has been assumed to be laminar. Since the magnetic Reynolds number (~ 0.001) is < 1, the induced current effect is very weak, allowing the internal electrical induction of the magnetic field to be neglected.

Therefore, the explicit semi-analytical solution was obtained. The resulting induced magnetic and electrical effects are implemented using user-defined functions (UDF).

Table II. Reynolds numbers calculated for each gas

No.	Boundary	Flow rate	Reynolds number
1	Inlet 1	$\dot{Q}_1 = 1$slpm	508,0292
2	Inlet 2	$\dot{Q}_2 = 3$slpm	95,25548
3	Inlet 3	$\dot{Q}_3 = 31$ slpm	492,1533

$$\left(\frac{\partial\vec{A}}{\partial t}\right)_{\text{rms}} = \sqrt{\int_0^{2\pi/w}\frac{\partial\vec{A}}{\partial t}\cdot\frac{\partial\vec{A}}{\partial t}dt} = \frac{1}{\sqrt{2}}w\vec{A}_{\text{rms}} = \frac{1}{\sqrt{2}}(2\pi f)\vec{A} \quad (6)$$

$$\sigma\left(\frac{\partial\vec{A}}{\partial t}\cdot\frac{\partial\vec{A}}{\partial t}\right) = \frac{1}{2}\sigma w^2\vec{A}\cdot\vec{A} \quad (7)$$

Gases are introduced into the plasma torch through three different sections: the carrier gas, the plasma gas, and the sheath gas. Each gas inlet is defined as an inlet boundary condition. The outlet boundary condition is defined at the exit of the plasma tube, where gases (25 cm long) from the reaction region are taken. All inlet boundaries and the gas feeding flow rates into the system are specified in Table II. Since the operating pressure is close to atmospheric pressure, the outlet boundary is defined with the default value of 1 atm. The inlet temperature of argon gas in the system has been set to 300 K in the modeling simulations.

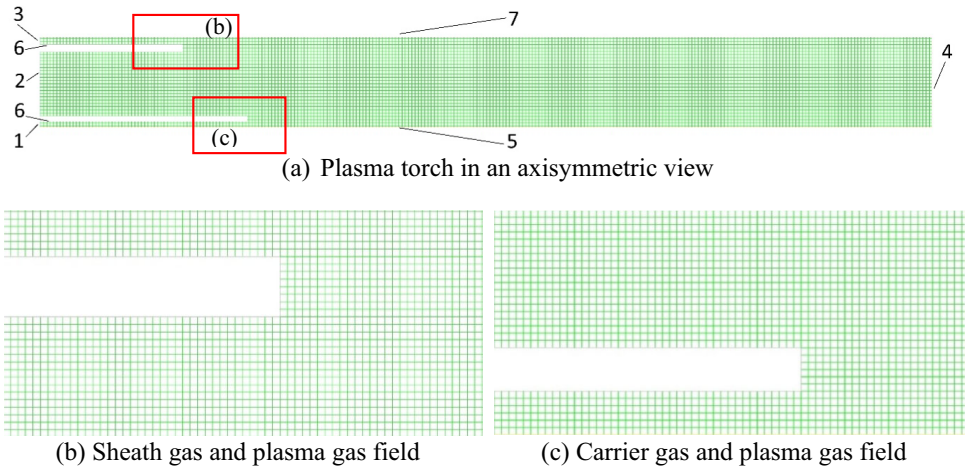
After defining the geometry, the numerical analysis generated the structured mesh for the plasma region. In Fig. 2, (a) the entire plasma torch in an axisymmetric view, (b) the mesh view of the carrier gas and plasma gas field, and (c) the mesh view of the sheath gas and plasma gas field are shown.

The mesh independence study for torch plasma modeling was repeated for seven different mesh counts, as shown in Fig. 3. In the mesh independence study, plasma did not form for Mesh 1, which has a low mesh count. For mesh 2 and mesh 3, the predicted plasma power was below the expected values. The mesh count values between meshes 4 and 7 provided accurate analysis results. To ensure an appropriate mesh count and reduce long processing times, mesh 6 was selected as the analysis mesh.

The boundary conditions and thermal conditions are provided in Table III. The flow rates of the argon gases entering the torch, as reported in the studies by Xue et al.[33] and Christian Busse et al.,[27] are as follows: the carrier gas flow rate is 1 slpm, the plasma gas flow rate is 3 slpm, and the sheath gas flow rate is 31 slpm.

Powder Modeling Approach

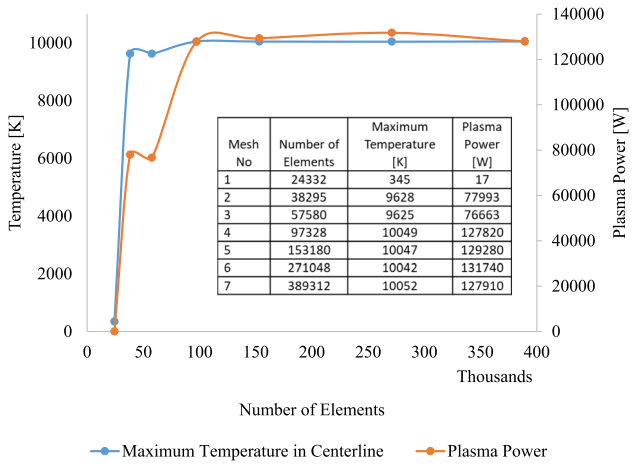
The spheroidization of powders is crucial for additive manufacturing technologies to produce products with superior properties. The RF plasma system, which does not require electrodes and generates plasma at high temperatures, enables high-melting-point titanium powders to pass through the plasma and cool, facilitating effective sinterization.[34] A review of the experimental and numerical studies in the literature reveals that the



(a) Plasma torch in an axisymmetric view

(b) Sheath gas and plasma gas field (c) Carrier gas and plasma gas field

Fig. 2. Mesh of the RF plasma spheroidization system. (a) Plasma torch in an axisymmetric view. (b) Sheath gas and plasma gas field. (c) Carrier gas and plasma gas field.



Mesh No	Number of Elements	Maximum Temperature [K]	Plasma Power [W]
1	24332	345	17
2	38295	9628	77993
3	57580	9625	76663
4	97328	10049	127820
5	153180	10047	129280
6	271048	10042	131740
7	389312	10052	127910

Fig. 3. Mesh independence for the torch.

Table III. Boundary conditions of the RF plasma spheroidization system

No	Boundary	Boundary condition	Thermal boundary condition
1	Inlet 1	$\dot{Q}_1 = 1$slpm	T = 300 K
2	Inlet 2	$\dot{Q}_2 = 3$slpm	T = 300 K
3	Inlet 3	$\dot{Q}_3 = 31$slpm	T = 300 K
4	Outlet	Pressure P = 1 atm	Adiabatic
5	Axis	–	–
6	Wall 1	No slip	Adiabatic
7	Wall 2	No slip	Convection h = 1000 W/m^{2}K T = 400 K

powder sizes used are generally limited to values of approximately ≤ 200 μm.

Titanium alloys are one of the most widely used metals in industrial applications. They are frequently used in the aerospace and healthcare sectors because of their properties, such as excellent corrosion resistance and biocompatibility.[35,36] Titanium is an essential metal characterized by its high melting point and high strength/density ratio.[37] With the development of additive manufacturing technologies, the application of titanium alloy powders has been expanded. This situation has increased demand for powders with improved properties. In industrial implementations, titanium and titanium alloys are required to have high sphericity, low oxygen content, high density, and controllable size.[38,39]

In spheroidization, carrier gas transports Ti powder to the plasma torch. When Ti powder absorbs enough heat in the plasma torch, it melts into spherical droplets, either fully or partially. The Ti droplets exiting the torch are cooled in the cooling chamber, and due to the high surface tension, they solidify into spherical shapes and fall into the powder collector.

$$\underset{\text{I}}{\rho \frac{\partial (c_P T)}{\partial t}} = \underset{\text{II}}{\vec{\nabla} \cdot \left(k \vec{\nabla} T \right)} \tag{8}$$

Equation 8 is the heat conduction equation for metal powder simulation. Term **I** is the transient term. Term **II** is the heat conduction term. c_P is the specific heat of metal powder, T is the temperature, and k is the thermal conductivity of metal powder.

In the numerical analysis, the following key assumptions were made when developing the particle model: (1) The particles are assumed to be spherical in shape; (2) it is assumed that the particles' velocity is the same as that of the carrier gas. The powder particles are injected into the torch

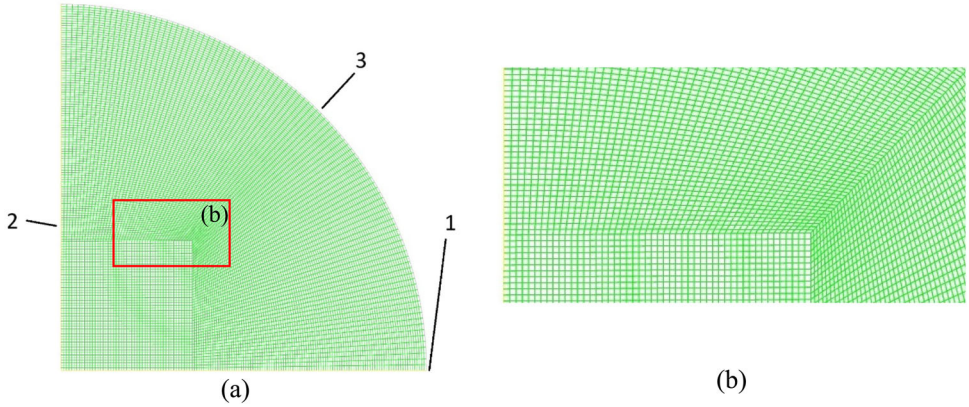


Fig. 4. (a) The mesh of the Ti particle affected by the plasma. (b) Detailed view of mesh the Ti particle center.

center along with the carrier gas, assuming velocity equilibrium ($v_{particle} = v_{gas}$) at the inlet. The terminology "carrier gas flow rate" (measured in slpm) is used consistently to define the volumetric flow that dictates initial particle momentum; (3) the motion of the particles is influenced only by gravitational and thermophoretic forces, with other forces neglected; (4) it is assumed that the particles move along a straight path; (5) the processes of melting, evaporation, and re-solidification of the particles are not considered. To focus on the heat transfer efficiency between the plasma and the coarse 400-μm particles, phase change kinetics (latent heat) are not explicitly modeled. Instead, the particle's ability to reach and maintain its melting temperature (T_m) throughout its volume is used as the criterion for spheroidization feasibility, a method established in fundamental literature by Boulos et al.[40] (6) the behavior of the particles does not affect the plasma's flow and temperature fields; (7) particle-particle interactions are not considered. After the geometry is defined according to the assumptions, the structured mesh for the plasma region is generated. Figure 4a shows the mesh of the Ti particle affected by the plasma and (b) a detailed mesh view of the Ti powder center. This mesh configuration is referred to as the O-grid. It provides a very high orthogonal quality and low skewness when generating mesh structures for circular and complex geometries.

Figure 5 shows the mesh independence studies for a 400-μm sized Ti particle. For the particle mesh structure, the numerical stability Fourier number ($\alpha^*\Delta t/\Delta x^2$) reaches approximately 0.3. Therefore, a tiny time step has been chosen for all analyses. For second-order limited time stepping, a Fo number $<$ 10 suffices, and a value $<$ 1 ensures a high-quality solution. The error margin after 12,500 iterations becomes very low; thus, mesh 5 is selected.

In this study, the properties of Ti powder are defined in Fluent. The effect of the plasma field on a Ti powder particle, which is fed into the system along with the carrier gas, has been examined as it

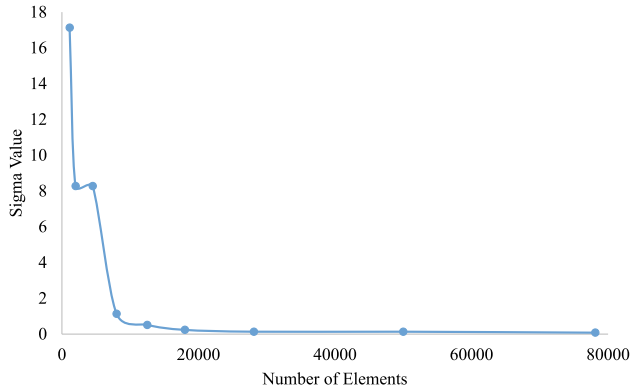


Fig. 5. Mesh independence for the Ti particle.

Table IV. Boundary conditions Ti power

No.	Boundary condition	Thermal boundary condition
1	Axis	–
2	Symmetry	$\frac{\partial T}{\partial x} = 0$
3	Wall	Radiation ε = 0.9 T = 8700 K

travels in a straight line through the torch geometry until it exits the torch. According to the findings from the plasma analysis, as given in Table IV, the average plasma temperature along the distance from the point where the Ti powder is first exposed to heat to the torch exit is 8700 K.

Considering that the melting temperature of titanium is $\sim$ 1940 K and the boiling temperature is $\sim$ 3560 K, the aim is to determine the carrier gas flow rate to ensure spheroidization of titanium powders within this temperature range.

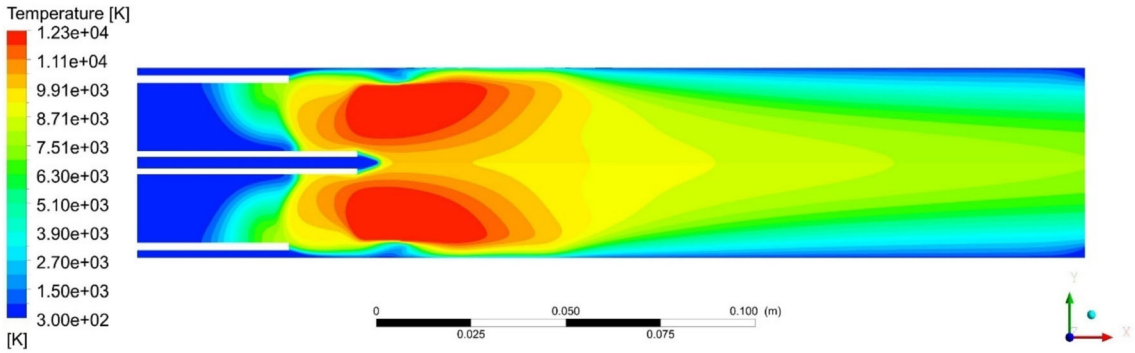


Fig. 6. Temperature distribution of plasma in the torch.

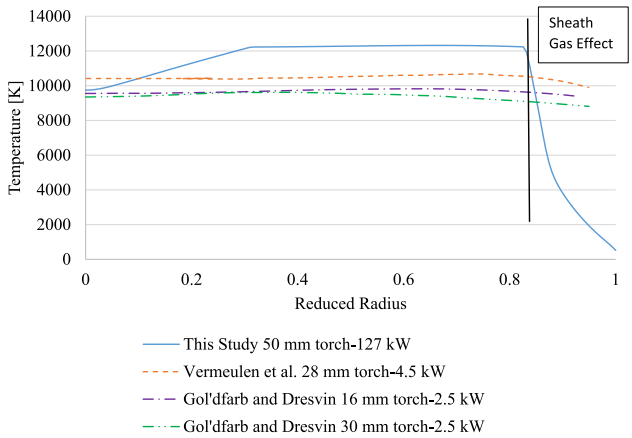


Fig. 7. Validation of temperature and power along the radius.

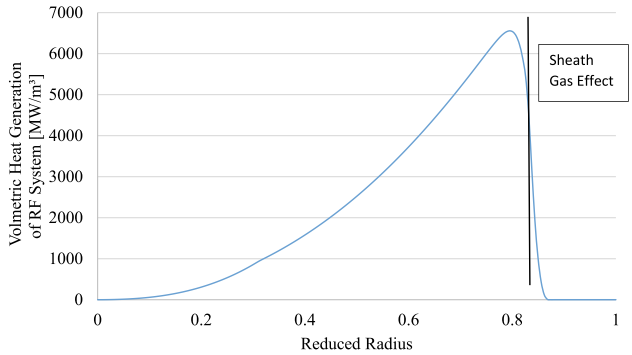


Fig. 8. Validation of volumetric heat generation of the RF system along the radius.

RESULTS AND DISCUSSION

The temperature distribution of the argon plasma obtained for a power of 125 kW and a frequency of 4 MHz is shown in Fig. 6. Many numerical studies in the literature show that the maximum temperatures of the plasma generated within the torch are around 10,000 K.[12,33,34] The results of our analysis indicate that the temperature distributions are comparable to those reported in previous studies. Due to the higher power used in our plasma analyses, the maximum temperature exceeds that reported in these studies, reaching 12,300 K inside the torch. High temperatures are observed in the region where the plasma induction coils are located. When surrounded by induction coils, a much higher ion and electron density can be induced by the oscillation of the electromagnetic field at high frequencies. Furthermore, as observed in previous studies, the maximum temperature in the system is not located along the central axis of the quartz tube. Due to the skin effect, it is in a region different from the center.[12]

Validation studies were conducted for torch analyses. In the validation studies, the comparisons of power, reduced radius, and temperature are presented in Fig. 7. The obtained results were compared with the experimental studies of Vermeulen et al.[41] and Gol'dfarb and Dresvin.[42] The results are consistent with the findings in the respective papers; however, the effects of the sheath gas caused additional cooling. The decrease observed for reduced radius values ≥ 8 can be attributed to the inclusion of the sheath gas effect in our study, in addition to the works of Vermeulen et al., Gol'dfarb, and Dresvin. The sheath gas effect is crucial for protecting the outer surfaces of the torch from high temperatures.

A comparison of the volumetric heat generation of the RF system and the reduced radius is provided in Fig. 8. The volumetric heat generation of the RF system matches the results of Vermaulen qualitatively. Since this article focused on industrial high-power systems, plasma power and temperature are higher than those of small RF torches.

To further validate the CFD model, the plasma temperature distribution along the centerline ($r = 0$) was compared with established models by Xue et al.[33] and Busse et al.[43] As illustrated in Fig. 9, the high level of agreement with previously reported studies validates the reliability of the developed UDF code for predicting the thermal environment.

Vortices that form in plasma environments are complex structures, and dynamics arise from electromagnetic and hydrodynamic interactions within the plasma. Velocity gradients and magnetic fields

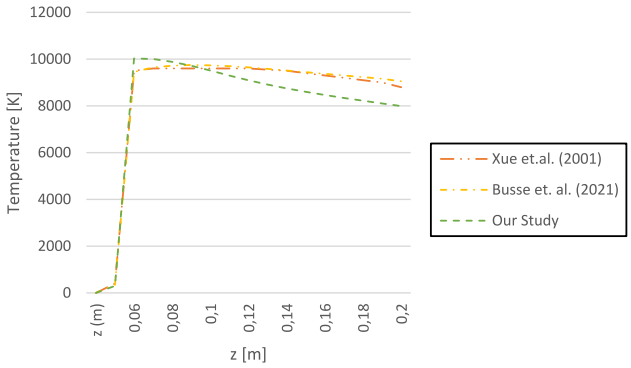


Fig. 9. Comparison of the plasma temperature distribution along the centerline (r:0).[33,43]

within the plasma flow typically drive these vortices. The movement of electric charges in the plasma interacts with the magnetic fields, creating density and velocity differences and forming vortex-like structures. These structures are particularly associated with physical phenomena such as plasma transport processes, energy transfer, and velocity differences, especially in regions of magnetic reconnection. The behavior of vortices varies depending on the type of plasma, the environmental temperature and density, and the injection of gases at different velocities into the same medium.

Furthermore, plasma vortices interact with dynamic processes such as turbulence, wave motion, and plasma waves, thereby contributing to the system's overall energy dynamics. Such structures play a crucial role in understanding the structure of magnetic fields and the linear and nonlinear characteristics of plasma flow. However, in our analysis, since we assume laminar flow, the vortices formed result from mixing gases with different velocities in the plasma environment and the influence of coils on the plasma near the exit region, as shown in Fig. 9.

In Eq. 9, a marked logarithmic graph similar to the logarithmic axis graph has been created. Due to the markings, the direction of the vortex's rotation can also be observed in Fig. 10. In the equation, ω represents the curl of the fluid's velocity, indicating the rotation of the flow.

$$\mathrm{Slog}_{10}(\omega) = \mathrm{sign}(\omega)\log_{10}(1+|\omega|) \tag{9}$$

The vortex formed in Fig. 10a is due to the Lorentz force. This region is situated between the coil's starting point and the area where the gases mix, resulting in a clockwise vortex. Figure 10b shows a different vortex region after the coil. Due to fluid friction, a counterclockwise vortex is created in this region, mixing the plasma gas with the powder.

In an argon plasma environment, the velocity distributions within a glass tube with gas inlets at three locations and varying flow rates exhibit a complex structure that depends on the gas inlet directions, plasma properties within the tube, and local flow conditions. Introducing gas from three distinct points results in non-homogeneous and interactive velocity profiles within the tube. Initially, each gas inlet generates a localized velocity component within the tube. As these velocity components move away from the tube walls and interact with the plasma, they are modulated by magnetic and electric fields. The gas flow at these inlet boundaries results in velocity distributions that vary depending on the ionization degree, temperature, and density differences within the plasma environment. As the temperature of the gas inside the tube increases, the velocities of the gas molecules exhibit greater dispersion; however, due to plasma effects, these velocities change between the center and the walls of the tube.

Furthermore, plasma density and temperature gradients create tendencies for acceleration or deceleration within the tube. The presence of ionized argon gas and its movement, as well as the electrical and magnetic interactions that develop within the tube, cause the velocity distribution to evolve dynamically. As shown in Fig. 11, the velocity distribution inside the tube changes because of interactions among the gas inlet zones, energy and momentum transfer within the plasma environment, and the influence of the coil.

The carrier gas, plasma gas, and carrier gas separated by quartz tubes enter the plasma environment inside the torch at a temperature of 300 K. As shown in Fig. 12, the locations where the temperature is observed are different for each of the three different flow rates of argon gas. Among these gas inlets, the plasma gas enters at 300 K, followed by the sheath and the carrier gas.

The relationship between carrier gas velocity and spheroidization is governed by the "thermal soak" requirements. At flow rates $>$ 4 slpm, higher velocities lead to a thermal bypass where the residence time (t_{res}) is shorter than the thermal penetration time (t_{cond}) required for the 400-μm particle's core to melt.

It is assumed that the three different flow rates of argon gas are unaffected by gas mixing regions, temperature and velocity differences, or vortices. When the gases travel along a straight line, the temperature distribution from the center of the gases along the x-direction, from the point of entry into the torch to the end of exit, is presented in the graph shown in Fig. 13.

Based on the results of the analysis studies, the temperature distribution of 400-μm titanium powder as it enters the plasma region at different flow rates is presented in Fig. 14. An increased flow rate reduced the titanium powder's residence time in the high-temperature zone. In this case, when the feeding rate of titanium powder to the torch is low, the temperature difference between the center and the outer surface of the powder is reduced. As the feeding rate of the powder increases, the temperature difference between the outer surface and the center of the powder becomes larger.

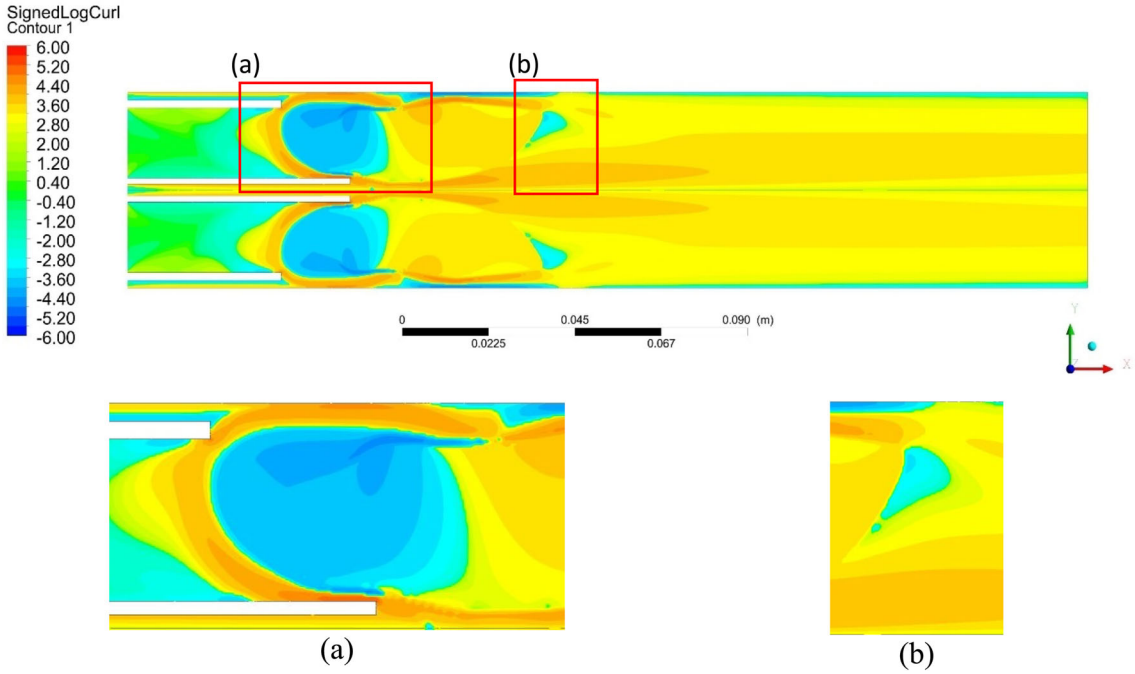


Fig. 10. The flow of gases within the plasma field and the vortices. (a) Detailed view of vortex formation in the coil region; (b) detailed view of vortex formation downstream of the coil.

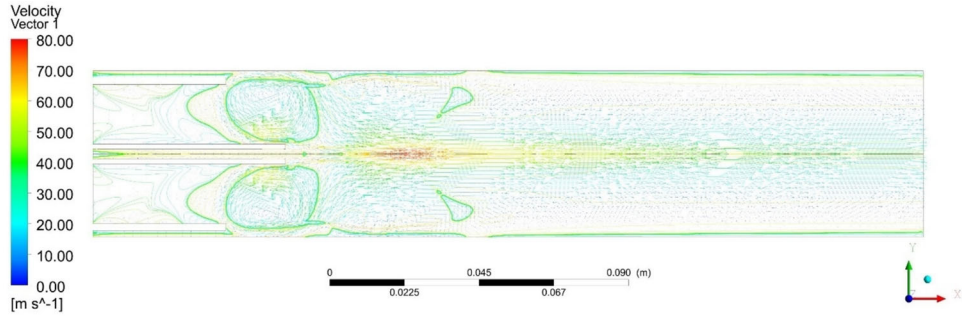


Fig. 11. The gas flow and velocity distribution.

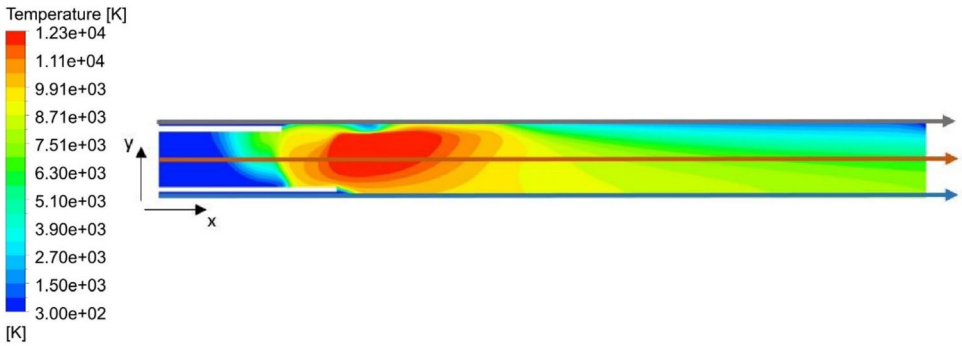


Fig. 12. Temperature distribution of plasma.

The temperature distribution profiles over a 20-cm distance, from the point of initial exposure to the torch exit, are also provided in Fig. 15. The primary objective of this study is to identify the "process window" by tracking the particles' thermal history. We use the melting temperature (Tm) as a

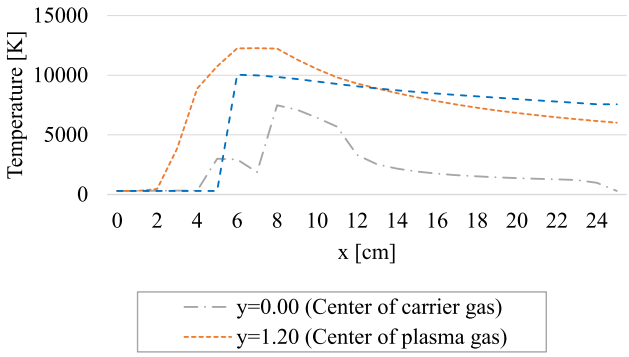


Fig. 13. Temperature variation along the x-axis at y = 0.0.

necessary thermal condition for spheroidization. By showing that a particle reaches Tm and stays below Tb (boiling point) within the plasma, we demonstrate that the plasma environment provides sufficient energy flux to facilitate phase change. By not including latent heat, our model predicts a maximum potential temperature. If a particle does not even reach Tm in this simplified model, it certainly will not melt in reality. Therefore, our optimal flow rate (2–4 slpm) remains a valid threshold for ensuring that the particle absorbs enough energy to enter the liquid phase.

In thermal plasma spheroidization studies, it is useful to introduce a dimensionless parameter that quantifies whether a particle has sufficient time to complete capillary-driven reshaping while traveling

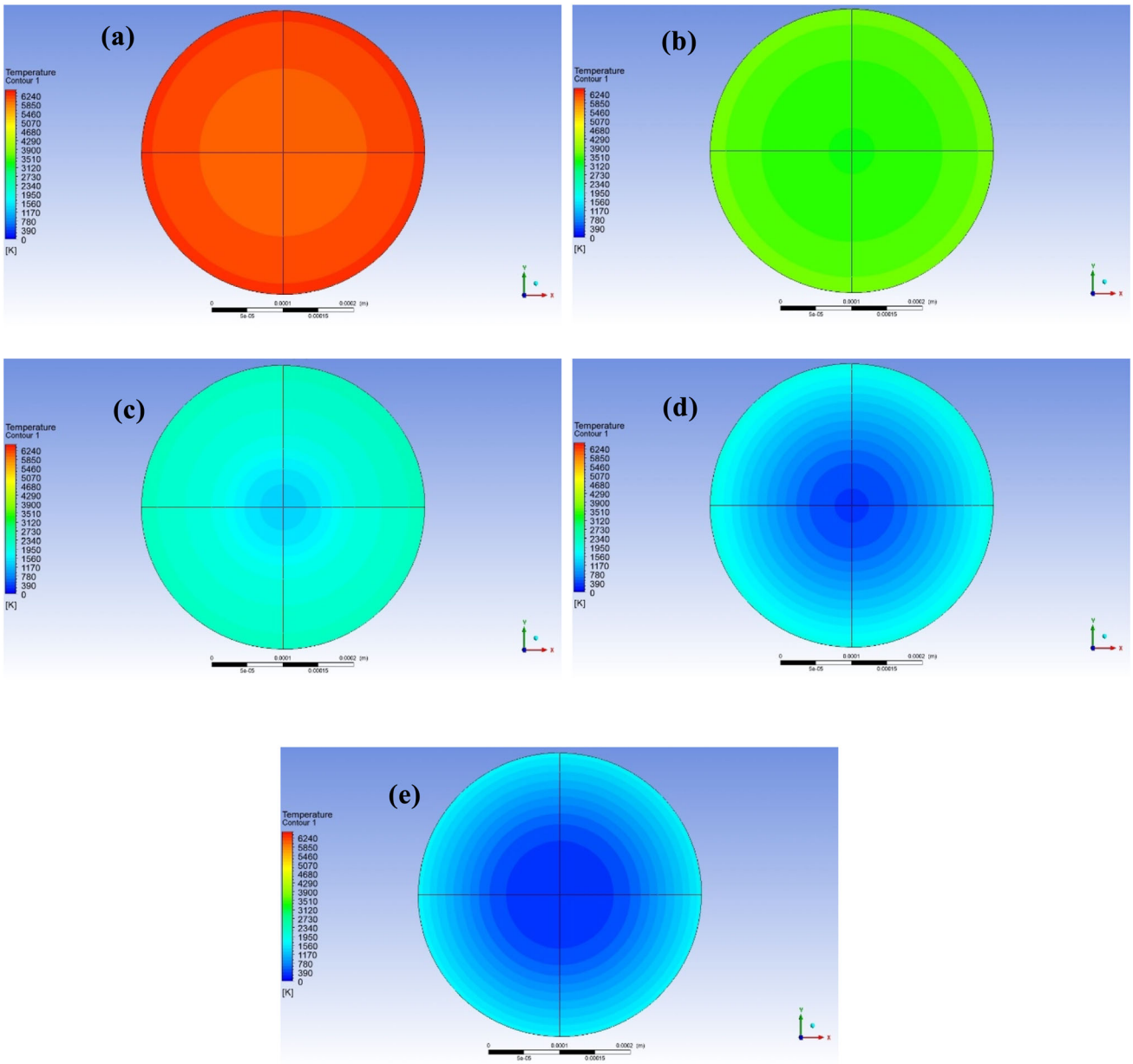


Fig. 14. The temperature distribution of 400-μm Ti powder at different feeding rates: (a) 1 slpm, (b) 2 slpm, (c) 4 slpm, (d) 7 slpm, (e) 10 slpm.

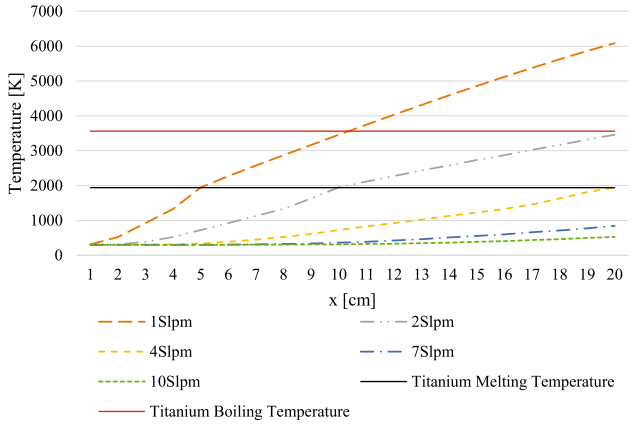


Fig. 15. Temperature distribution of 400-μm titanium powder at different powder-feeding gas flow rates.

through the high-temperature region of the plasma. This parameter is referred to as the spheroidization sufficiency ratio (SSR). The SSR compares the actual residence time of a particle in the plasma with the minimum time required for the molten particle to relax into a spherical shape due to surface tension forces. It can be expressed as:

$$\mathrm{SSR} = \mathrm{tres}/\mathrm{treq} \tag{10}$$

Here, t_{res} is the particle residence time in the high-temperature plasma region, and t_{req} is the characteristic time required for a molten particle to achieve a spherical morphology through capillary relaxation. The required spheroidization time is commonly estimated from capillary relaxation theory, which relates the reshaping dynamics of a liquid droplet to the balance between surface tension and inertial forces. The value of SSR provides a convenient criterion for assessing spheroidization conditions. When SSR $<$ 1, the particle does not remain in the plasma long enough to complete capillary reshaping, resulting in partially molten or irregular morphologies. When SSR $\approx$ 1, the particle is at the threshold of spheroidization. For SSR $\gg$ 1, the particle has sufficient time to fully relax into a spherical shape before leaving the plasma region.

Because the required time scales approximately with ($t_{req} \propto d_p^{3/2}$), larger particles demand significantly longer residence times to achieve spheroidization. Consequently, SSR is particularly useful in the process modeling and design of plasma spheroidization systems, as it links particle size, thermophysical properties, and reactor hydrodynamics into a single dimensionless parameter that predicts the likelihood of producing highly spherical powder. Table V presents the distance at which the center of a 400-μm particle reaches its melting temperature and provides an assessment of the particle's condition. After analyzing the data in the table, the carrier gas flow rate at which the SSR value would exceed 1 was determined. From this perspective, 2–4 slpm carrier gas flow rates are suitable for spheroidizing a 400-μm particle.

When the titanium powder exits the torch, the temperature at its center exceeds 6000 K, significantly above the vaporization temperature, at a flow rate of 1 slpm. At 2- and 4-slpm flow rates, the powder remains within the melting and boiling temperature range. In contrast, at 7- and 10-slpm flow rates, the temperature remains below the melting point, indicating that the powder does not completely melt; rather, only its surface melts.

CONCLUSION

In numerical analysis studies, electromagnetic fields and fluid flow have been modeled, yielding temperature and velocity distributions. The effects of this plasma environment on the temperature of titanium particles were determined. UDF codes were created and defined in the Fluent program to generate RF plasma. The impact of this plasma environment on the temperature of titanium particles was investigated using various carrier gas flow rates. As a result of the numerical analyses, the following conclusions can be drawn:

- In the RF ICP plasma system, by carefully adjusting the essential parameters, such as plasma power, frequency, gas properties, and flow rates, suitable conditions for the spheroidization of titanium powders can be achieved. Furthermore, these numerical studies have demonstrated that suitable plasma environments can be created to produce spherical powders, which are essential for additive manufacturing.
- The results show that spheroidization of Ti powder with a relatively large size of 400 μm can be achieved at a high power level of 125 kW and a frequency of 4 MHz. These conclusions are specifically applicable to the 125-kW RF plasma system architecture. The identified optimal window of 2–4 slpm results from the balance between the 400-μm Ti particle's thermal inertia and the torch's specific residence time characteristics. Changes in feedstock material properties or torch geometry would necessitate recalibrating these flow parameters.
- As a result of the investigation into the effects of carrier gas flow rate on particle temperature within the same plasma environment, an optimal carrier gas flow rate can be determined. It is observed that high particle velocities prevent attaining the necessary temperature for melting, while low velocities may cause the temperature to exceed the boiling point. These results indicate that the feeding gas flow rate can be determined for a specific powder size range to achieve powder temperatures within the powder's melting and boiling ranges.
- Departing from traditional laboratory-scale investigations, the present work establishes a specialized operational envelope for 125-kW industrial RF systems, effectively bridging the

Table V. Quantitative data for the 400-μm Ti particle for spheroidization assessment

Carrier gas flow rate (Q) [slpm]	Distance to reach core melting point (~1940 K) [cm]	Max. particle core temperature ($Tcore$) [K]	Vaporization risk ($T > 3560$ K)	Spheroidization sufficiency status
1	≈ 5.0	> 6000	Extreme	Insufficient (high mass loss)
2	≈ 11.0	≈ 3400	None	Fully sufficient (optimal)
4	≈ 19.5	≈ 2400	None	Fully sufficient (optimal)
7	Not reached	≈ 1000	None	Insufficient (partial/surface only)
10	Not reached	≈ 600	None	Insufficient (incomplete melting)

technical void in coarse powder processing through a rigorous methodological framework based on UDF-integrated electromagnetic modeling.

- For the spheroidization of powder particles, particle size and the exposure times to high temperatures within the torch are critical parameters. The exposure times at high temperatures for relatively large Ti particles (400 μm) were investigated as the flow rate was varied. The ideal flow rate ranges for the spheroidization of 400-μm Ti powder have been determined; flow rates between 2 and 4 slpm kept the particles within the melting and boiling temperature ranges. However, at flow rates < 2 slpm, the residence time in the hot zone was sufficiently long to allow the Ti particles to exceed their boiling point. On the other hand, for flow rates > 4 SLPM, the Ti particles remained below the melting point. Based on the findings, the effects of flow rates on 400 μm Ti particles have been determined.
- The RF plasma system demonstrates significant potential for additive manufacturing, powder metallurgy, and materials engineering. Further research is required to thoroughly explore and optimize its capabilities in these areas.

ACKNOWLEDGEMENTS

We would like to express our sincere appreciation to the Scientific and Technological Research Council of Turkey (TÜBİTAK) for their financial support of the SAYEM research project (project grant no. 3219504-121D013). Their funding played a crucial role in the successful execution of this study and in achieving our research goals.

On behalf of all authors, the corresponding author states that there is no conflict of interest.

FUNDING

Open access funding provided by the Scientific and Technological Research Council of Türkiye (TÜBİTAK). Türkiye Bilimsel ve Teknolojik Araştırma Kurumu, 3219504-121D013, IRFAN ÜNAL, 3219504-121D013, Rahmi Ünal.

OPEN ACCESS

This article is licensed under a Creative Commons Attribution 4.0 International License, which permits use, sharing, adaptation, distribution and reproduction in any medium or format, as long as you give appropriate credit to the original author(s) and the source, provide a link to the Creative Commons licence, and indicate if changes were made. The images or other third party material in this article are included in the article's Creative Commons licence, unless indicated otherwise in a credit line to the material. If material is not included in the article's Creative Commons licence and your intended use is not permitted by statutory regulation or exceeds the permitted use, you will need to obtain permission directly from the copyright holder. To view a copy of this licence, visit http://creativecommons.org/licenses/by/4.0/.

REFERENCES

1. H. Duan, X. Liu, X. Ran, J. Li, and D. Liu, *Int. J. Miner. Metall. Mater.* https://doi.org/10.1007/s12613-017-1492-4 (2017).
2. M.Ç. Tüzemen, E. Salamcı, and R. Ünal, *Mater. Today Commun.* https://doi.org/10.1016/j.mtcomm.2022.103592 (2022).
3. A.M. Dursun, M.Ç. Tüzemen, E. Salamci, O. Yilmaz, and R. Ünal, *Politeknik Derg.* https://doi.org/10.2339/politeknik.891080 (2022).
4. J. Zhu, H. Zhou, C. Wang, L. Zhou, S. Yuan, and W. Zhang, *Chin. J. Aeronaut.* 34(1), 91 https://doi.org/10.1016/J.CJA.2020.09.020 (2021).
5. Y. Karabulut, and R. Ünal, *J. Mater. Sci.* https://doi.org/10.1007/s10853-022-07850-0 (2022).
6. Z. Hao, et al., *Int. J. Refract. Met. Hard Mater.* https://doi.org/10.1016/j.ijrmhm.2021.105624 (2021).
7. Q. Qin, et al., *Adv. Powder Technol.* 30(8), 1709 https://doi.org/10.1016/j.apt.2019.05.022 (2019).
8. H.-C. Zhu, et al., *Appl. Therm. Eng.* 281, 128607 https://doi.org/10.1016/J.APPLTHERMALENG.2025.128607 (2025).

9. A. Jankeviciute, Z. Károly, N.V. Tarakina, J. Szépvölgyi, and A. Kareiva, *J. Non Cryst. Solids* 359(1), 9–14 https://doi.org/10.1016/j.jnoncrysol.2012.09.025 (2013).
10. I. Mohai, and J. Szépvölgyi, *Chem. Eng. Process. Process Intensif.* 44(2), 225–229 https://doi.org/10.1016/j.cep.2004.04.008 (2005).
11. J.S. Nam, E. Park, and J.H. Seo, *Met. Mater. Int.* 26(4), 491–500 https://doi.org/10.1007/S12540-019-00348-6/TABLES/4 (2020).
12. J.B. Tong, X. Lu, C.C. Liu, Z.Q. Pi, R.J. Zhang, and X.H. Qu, *Appl. Therm. Eng.* 100, 1198–1206 https://doi.org/10.1016/J.APPLTHERMALENG.2016.02.108 (2016).
13. D.V. Ivanov, and S.G. Zverev, *IEEE Trans. Plasma Sci.* 50(6), 1700–1709 https://doi.org/10.1109/TPS.2022.3175741 (2022).
14. Y. Cheng, M. Shigeta, S. Choi, and T. Watanabe, *Chem. Eng. J.* 183, 483–491 https://doi.org/10.1016/j.cej.2011.12.040 (2012).
15. N. Kobayashi, et al., *Thin Solid Films*. https://doi.org/10.1016/j.tsf.2007.10.064 (2008).
16. Z. Yan, M. Xiao, X. Mao, K. Khanlari, Q. Shi, and X. Liu, *Powder Technol.* 385, 160 https://doi.org/10.1016/j.powtec.2021.02.075 (2021).
17. J. Guo, X. Fan, R. Dolbec, S. Xue, J. Jurewicz, and M. Boulos, *Plasma Sci. Technol.* 12(2), 188 https://doi.org/10.1088/1009-0630/12/2/12 (2010).
18. K.A. Khor, L.G. Yu, Y. Li, Z.L. Dong, and Z.A. Munir, *Mater. Sci. Eng. A*. https://doi.org/10.1016/S0921-5093(02)00151-X (2003).
19. J.L. Xu, K.A. Khor, Y.W. Gu, R. Kumar, and P. Cheang, *Biomaterials*. https://doi.org/10.1016/j.biomaterials.2004.06.042 (2005).
20. J. Hyesook, H. Chulwoong, K. Byungmoon, K. Dohyang, and C. Hanshin, Interface activated sintering of tungsten by nano-particles in the spark plasma sintering, in *Reviews on Advanced Materials Science*, 2011, vol. 28, no. 2.
21. X.L. Jiang, and M. Boulos, *Trans. Nonferrous Met. Soc. China* 16(1), 13 https://doi.org/10.1016/S1003-6326(06)60003-4 (2006).
22. R. Li, et al., *Adv. Powder Technol.* 28(12), 3158–3163 https://doi.org/10.1016/j.apt.2017.09.019 (2017).
23. E. YURTKURAN, W. K. W. SUNJUQ, A. ÖZSUNAR, and R. ÜNAL *Gazi Üniversitesi Mühendislik-Mimarlık* Fakültesi Derg., vol. 33, no. 1, 2018, https://doi.org/10.17341/gazimmfd.406807.
24. E. Yurtkuran, and R. Ünal, *Trans. Nonferrous Met. Soc. China (English Ed.* 32(1), 175 https://doi.org/10.1016/S1003-6326(21)65786-2 (2022).
25. J. He, L. Bai, H. Jin, and F. Yuan, *Powder Technol.* 302, 288 https://doi.org/10.1016/j.powtec.2016.08.067 (2016).
26. H. Zhu, H. Tong, C. Cheng, and N. Liu, *Int. J. Refract. Met. Hard Mater.* https://doi.org/10.1016/j.ijrmhm.2017.01.017 (2017).
27. C. Busse, I. Tsivilskiy, J. Hildebrand, and J.P. Bergmann, *Comput. Fluids* 216, 104807 https://doi.org/10.1016/J.COMPFLUID.2020.104807 (2021).
28. Q. Xin, X. Su, S. Alavi, B. Wang, and J. Mostaghimi, *Appl. Therm. Eng.* https://doi.org/10.1016/j.applthermaleng.2017.07.131 (2018).
29. Y.C. Lee, Y.P. Chyou, and E. Pfender, *Plasma Chem. Plasma Process.* 5(4), 391 https://doi.org/10.1007/bf00566011 (1985).
30. Q. Zhang, D. Yu, F. Liu, X. Miao, J. Qiu, and Y. Fan, *Appl. Therm. Eng.* https://doi.org/10.1016/j.applthermaleng.2023.121031 (2023).
31. K.S. Sista, A.P. Moon, G.R. Sinha, B.M. Pirjade, and S. Dwarapudi, *Powder Technol.* 400, 117225 https://doi.org/10.1016/J.POWTEC.2022.117225 (2022).
32. E. Yurtkuran, and R. Ünal, *Plasma Chem. Plasma Process.* https://doi.org/10.1007/s11090-020-10095-x (2020).
33. S. Xue, P. Proulx, and M.I. Boulos, *J. Phys. D Appl. Phys.* 34(12), 1897https://doi.org/10.1088/0022-3727/34/12/321 (2001).
34. Z. Hao, Y. Chen, Q. Zhang, P. Wang, Y. Shu, and J. He, *Adv. Powder Technol.* https://doi.org/10.1016/J.APT.2021.11.031 (2022).
35. P. Sun, Z.Z. Fang, Y. Xia, Y. Zhang, and C. Zhou, *Powder Technol.* 301, 331 https://doi.org/10.1016/j.powtec.2016.06.022 (2016).
36. W.H. Wei, L.Z. Wang, T. Chen, X.M. Duan, and W. Li, *Adv. Powder Technol.* 28(9), 2431 https://doi.org/10.1016/j.apt.2017.06.025 (2017).
37. I. Gibson, D. W. Rosen, and B. Stucker, *Addit. Manuf. Technol. Rapid Prototyp. to Direct Digit. Manuf.*, pp. 1, 2010, https://doi.org/10.1007/978-1-4419-1120-9.
38. H. Zhang, L. Bai, P. Hu, F. Yuan, and J. Li, *Int. J. Refract. Met. Hard Mater.* 31, 33–38 https://doi.org/10.1016/j.ijrmhm.2011.09.002 (2012).
39. J.J. Wang, J.J. Hao, Z.M. Guo, and Y.M. Wang, *Rare Met.* https://doi.org/10.1007/s12598-014-0293-4 (2015).
40. M.I. Boulos, *IEEE Trans. Plasma Sci.* https://doi.org/10.1109/TPS.1978.4317100 (1978).
41. P.J. Vermeulen, W.L. Boddie, and F.A. Wierum, *AIAA J.* https://doi.org/10.2514/3.4116 (1967).
42. S. V. Gol'dfarb, V.M. and Dresvin, *High Temperature 3,303*. 1965.
43. C. Busse, I. Tsivilskiy, J. Hildebrand, and J.P. Bergmann, *Comput. Fluids*. https://doi.org/10.1016/j.compfluid.2020.104807 (2021).

Publisher's Note Springer Nature remains neutral with regard to jurisdictional claims in published maps and institutional affiliations.